



Tailoring the radiation tolerance of eutectic high-entropy alloy via phase-composition control

Y.H. Zhou^{a,b}, S.F. Liu^{a,b}, D. Chen^{c,*}, Q.F. Wu^d, B. Xiao^{a,b}, F. He^d, Z.J. Wang^d, T. Yang^e, J.J. Kai^{a,b,**}

^a Department of Mechanical Engineering, City University of Hong Kong, Hong Kong, China

^b Center for Advanced Nuclear Safety and Sustainable Development, City University of Hong Kong, Hong Kong, China

^c School of Energy and Environment, Southeast University, Nanjing, China

^d State Key Laboratory of Solidification Processing, Northwestern Polytechnical University, Xi'an, China

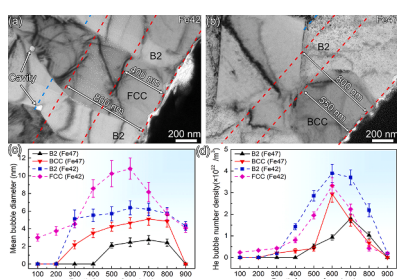
^e Department of Materials Science and Engineering, City University of Hong Kong, Hong Kong, China



HIGHLIGHTS

- Two kinds of EHEAs are designed by changing the relative content between Ni and Fe.
- Ordered B2 phase shows superior radiation tolerance to FCC and BCC phases.
- Strong radiation tolerance material can be designed by phase-composition control.

GRAPHICAL ABSTRACT



ARTICLE INFO

Keywords:

Eutectic high-entropy alloys
He ion irradiation
Alloy design
Radiation tolerance

ABSTRACT

Eutectic high-entropy alloys (EHEAs) take advantage of heterogeneous crystal structures, numerous interfaces, and multicomponent composition designs, implying a potential radiation tolerance in the nuclear environment. In this work, we employed the He ion irradiation to study the irradiation behavior of two types EHEAs ($\text{Fe}_{42}\text{Ni}_{31}\text{Al}_{17}\text{Cr}_{10}$, abbreviated as Fe42, and $\text{Fe}_{47}\text{Ni}_{26}\text{Al}_{17}\text{Cr}_{10}$, abbreviated as Fe47) with different phase designs. The results showed that the FCC + B2 constituted Fe42 EHEA and BCC + B2 constituted Fe47 EHEA retained their general phase-composition features up to ~ 1.2 dpa at 1073 K, while the long-range order of B2 phase was slightly disrupted in both alloys and more severe in the Fe42 EHEA. The quantification on He bubbles formation in different phases further indicated that the ordered B2 phase in Fe47 EHEA has a superior radiation resistance with smaller bubble size and less population. The differences in phase compositions and structures were believed to influence the vacancy-mediated helium diffusion during irradiation, which can account for the He bubble behaviors in the two kinds of alloys. The analysis on the width of bubble denuded zone along the phase boundary further suggested a higher energy barrier for the vacancy migration in the B2 phase, which consistently supported our inference on the underlying mechanism of bubble formation resistance of Fe47 EHEA. We believe that this work will provide a new strategy for designing EHEAs with excellent resistance to irradiation at elevated temperatures.

* Corresponding author.

** Corresponding author at: Department of Mechanical Engineering, City University of Hong Kong, Hong Kong, China.

E-mail addresses: dachen@seu.edu.cn (D. Chen), jijkai@cityu.edu.hk (J.J. Kai).

1. Introduction

As a low-carbon and high-efficient clean energy, nuclear power will play a more important role in the global mission of carbon neutrality. With the merits of fuel breeding, high efficiency, inherent safety, and reduction in waste generation, advanced nuclear systems including Generation IV reactors and D-T fusion reactors have been deemed as the inevitable courses for the sustainable development of nuclear energy. However, advanced nuclear energy systems were usually designed to operate at a high-temperature regime (up to 1000 °C) with unique coolants (e.g., liquid metals) and intense neutron flux [1–3]. The structural materials used in the cores of advanced reactors will face an unprecedented extreme environment combining high-energy neutrons radiation, intense thermomechanical stresses, and aggressive chemical corrosion [4]. In particular, the neutron irradiation-induced displacement damage and transmutation reactions will produce numerous point defects (interstitials and vacancies) and insoluble helium (He) atoms in the crystalline structure [5]. Along with the temperature effects and increased dose, the point defects can evolve into different microstructures, such as black dots, dislocation loops, voids, and helium bubbles, etc. [6–8]. These defects will further degrade the reactor materials' mechanical properties and dimensional stability via the low-temperature radiation hardening, segregation, high-temperature He embrittlement, and void swelling [9,10]. Therefore, the innovation of radiation-resistant materials has been a longstanding subject in nuclear material study.

Recently, high-entropy alloys (HEAs) with the multi-principal-element design have attracted broad attention in the materials community due to their superior mechanical properties, excellent oxidation/corrosion resistances, and promising radiation tolerance [11–14]. Up to now, various types of HEAs have been developed, including face-centered cubic (FCC) HEAs [15], body-centered cubic (BCC) HEAs [16], eutectic HEAs (EHEAs) [17], and the precipitation-hardened HEAs etc. [12,18]. The previous studies found that the radiation behaviors of single-phase HEAs were mainly affected by the composition complexity, the roughed energy landscape for point defect migration, and the chemical short-range order. For example, Zhang et al. [19] first reported that the radiation damage accumulation was gradually alleviated from the pure nickel to the single FCC phase concentrated solid solution alloys (CSSAs) of NiFe, NiCoFe, and NiCoFeCr. Ke et al. [20] and Lu et al. [21] further reported that the void swelling of Ni-based FCC CSSAs can be suppressed by increasing the chemical composition complexity. Chen et al. [22] and Zhao et al. [23] found that the featured energy barriers for the point defects migration in the FeCoNiCr HEA can promote the recombination of defects and reduce the vacancy concentration during irradiation, thereby suppressing helium diffusion and subsequent He bubble formation. The recent work by Lu et al. [24] found that the excellent radiation resistance of $Ti_2ZrHfV_{0.5}Mo_{0.2}$ BCC HEA should be related to its high vacancy concentration.

It has been well known that the BCC structure has an intrinsic radiation tolerance compared with the FCC structure, especially for void swelling [25]. However, the radiation-induced ductile-brittle transition temperature (DBTT) shift is another intractable issue for the ferritic alloys [26]. Therefore, the EHEAs comprising the two-phase structures may provide a new way to address the above dilemma. Moreover, the phase boundary of EHEAs can introduce numerous interfaces as additional sinks, which will benefit the radiation-induced point defects recombination. The radiation response of EHEAs was first reported by Xia et al. [27]. They found that the FCC phase in $Al_xCoCrFeNi$ EHEAs showed smaller volume swelling than that of the BCC phase, which exhibited a reverse trend compared with conventional nuclear materials. Pang et al. [28] studied the responses of FCC and B2 phases in $AlCoCrFeNi_{2.1}$ EHEA to the He irradiation at room temperature and 723 K. The FCC phase showed superior irradiation resistance to the B2 phase, which can be attributed to the complicated atomic-level lattice environment and compositional complexity of the FCC phase. Undoubtedly,

the irradiation behavior of EHEAs was relevant to their crystalline features and the specific chemical compositions. Revealing the effects of phase-composition on the irradiation behavior of EHEAs is of great importance for designing the new-type of radiation tolerant EHEAs.

In this work, we designed two kinds of Co-free EHEAs, i.e., $Fe_{42}Ni_{31}Al_{17}Cr_{10}$ (abbreviated as Fe42, in at.%) and $Fe_{47}Ni_{26}Al_{17}Cr_{10}$ (abbreviated as Fe47, in at.%) with distinct phase-composition features. The elevated temperature He ions irradiation was employed to study their irradiation resistance. The irradiated microstructures and He bubble formation in different phases of the designed EHEAs were carefully examined along the irradiation depth. The underlying reasons for their different irradiation behaviors were suggested in terms of chemical composition and crystalline structure. This work may contribute some valuable insights into the development of advanced nuclear structural materials.

2. Experimental

2.1. Materials and ion irradiation

The EHEAs were fabricated through arc melting the high-purity raw materials (purity > 99.95 wt.%) with the designed stoichiometry under an argon atmosphere. The ingot was remelted six times to achieve uniform chemical composition, and then dropped into a water-cooling copper mold to form a plate with a dimension of 5 mm × 10 mm × 100 mm. Before irradiation, the materials were cut into 3 mm × 3 mm × 2 mm blocks and then mechanically polished using SiC papers. The samples were further electrolytic polished in a mixed solution of HNO_3 : $C_2H_6O = 1:4$ for 40 s with a direct voltage of 20 V at the temperature of -40 ± 5 °C.

Irradiation experiment was conducted at the triple-beam ion irradiation system in National Tsing Hua University, using the 500 kV ion implanter (HVEE, model 80.20.002, Europe). The polished samples were irradiated by 275 keV He ions under a defocus beam model with a fluence of 5.14×10^{20} ions/m² under a vacuum of 5×10^{-5} Pa at 1073 K. The irradiation temperature was monitored by a thermocouple attached to the sample and an infrared thermometer gun. The ions fluence was measured by a Faraday cup installed behind of irradiation stage. The irradiation damage (displacements per atom, dpa) and He ion concentration along the incident direction were calculated using the Stopping and Range of Ions in Matter (SRIM-2013) with the Quick Kinchin-Pease Mode. The displacement energies were set as 40 eV for Fe, Cr, Ni, and 25 eV for Al [29]. Fig. 1(a) and (b) show the profiles of the irradiation damage and He concentration of phases in Fe42 and Fe47 EHEAs as a function of depth, respectively. The damage depths for the B2 phases in both Fe42 and Fe47 EHEAs are slightly deeper than those of FCC and BCC phases, respectively. While the He concentration profiles of the phases in both Fe42 and Fe47 EHEAs go behind their corresponding damage profiles.

2.2. Characterization

The cross-sectional samples used for transmission electron microscopy (TEM) analysis were fabricated using a focused ion beam workstation (FEI Scios microscope). The irradiated microstructures of samples were characterized by TEM (JEOL 2100F, operated at 200 kV). Phase compositions and crystallographic features were determined using energy dispersive spectrometer (EDS) and selected area electron diffraction (SAED) equipped on TEM, respectively. He bubbles in different phases were characterized by the through-focus TEM technique in a bright field mode, and the defocus value was fixed to -800 nm to ensure the same condition for the size comparison. To obtain the number density of He bubbles from the two-dimensional images, the convergent beam electron diffraction (CBED) technique was used to measure the sample thickness of TEM samples under the two-beam diffraction condition [30,31]. The details were provided in the supplementary material

(Fig. S.1).

3. Results

3.1. Microstructure of the irradiated Fe42 and Fe47 EHEAs

STEM experiments were first conducted to determine the microstructure, phase constitution and chemical composition of the irradiated Fe42 and Fe47 EHEAs. As shown in Fig. 2(a), the STEM BF image of Fe42 EHEA shows the typical eutectic microstructure with different contrasts, and the irradiated region is marked by the red dot lines. The SAED patterns in the insets of Fig. 2(a) and (b) illustrate that the dark area is mainly composed of a disordered FCC phase, while the light area mainly consists of an ordered B2 phase. A strong (100) superlattice spot can be observed in diffraction pattern of B2 phase, indicating a highly ordered structure of the B2 phase. To evaluate the irradiation on the ordering degree of B2 phase, the intensity profiles taken from the (110) diffraction spot and (100) superlattice spot of the irradiated and unirradiated B2 phases are shown in the insets of Fig. 2(b) and (c), respectively. The long-range ordering degree was evaluated by the relative intensity ratio of the (100) superlattice spot and (110) diffraction spot. It can be found that the ordering degree of the irradiated B2 phase had a decrease of ~16.7% compared with the unirradiated B2 phase. The EDS maps in Fig. 2(d) further show that FCC phase is rich in elements Fe and Cr, depleted in elements Ni and Al, while B2 phase is in a reverse situation. The composition features of the irradiated region did not show a visible variation. The detailed chemistry compositions of FCC and B2 phases are listed in Table 1.

Fig. 3 shows the irradiated microstructures of the Fe47 EHEA. Similar to the Fe42 EHEA, two distinct areas were identified based on the image contrast of the STEM-BF image. The irradiation area is marked by the red dot lines in Fig. 3(a). The SAED patterns in the inset of Fig. 3(a) and (b) confirmed a disordered BCC phase structure with gray contrast and an ordered B2 phase structure with light contrast, respectively. The variation of long-range ordering degree of the irradiated B2 phase was also evaluated as the displayed intensity profile crossing the (110) diffraction spot and (100) superlattice spot. The results showed that the ordering degrees of the irradiated B2 phases show a slight decrease of ~5.2%, compared with Fe42 EHEA. Fig. 3(d) shows the elemental distribution of the BCC phase and B2 phase in Fe47 EHEA, and corresponding chemical compositions are summarized in Table 1. It can be found that the B2 phase is mainly rich in elements Ni and Al, but the composition ratio between Ni:Al is closer to 1:1. The difference in composition of B2 phase between Fe42 and Fe47 EHEAs is thought as one of the main reasons for the change in ordering degree of B2 phase. Compared with FCC phase in Fe42 EHEA, the BCC phase in Fe47 EHEA possess similar chemical contents in elements Al and Cr, but varied in elements Fe and Ni. Element Ni has a significant effect on the phase transformation of Fe-Ni-Cr system alloys. High Ni content can stabilize

the FCC phase [32,33]. To demonstrate the effect of Ni content on phase transition during solidification, we calculated the isothermal cross-sectional phase diagram of Fe-Cr-Ni system at the latest stage of solidification (1673 K) using Thermo-Calc software (V2022b) and TCFE7: Steels/Fe-Alloys v7.0 database. As illustrated in Fig. 4, when the Cr content is fixed at 15 at.%, with the increase of Ni content, the primary solidification phase changes from BCC phase to FCC phase, which is consistent with the results of this work.

3.2. Helium bubble behavior in the Fe42 and Fe47 EHEAs

Fig. 5(a) and (b) show the overall He bubble distribution in Fe42 and Fe47 EHEAs along the depth direction, respectively. Most of the He bubbles were densely distributed in the depth range of 400–800 nm for both the FCC and B2 phases in Fe42 EHEA, while extra He bubbles can be found in the B2 phase deeper than 800 nm (area between the red and blue dash lines), which is consistent with the prediction of SRIM simulation. Some cavities with faceted structures were found to be decorated at the phase boundary beyond the irradiation range. The reason might be attributed that the boundary structure can be an efficient diffusion channel for radiation-induced excess vacancies, while the implanted He was mostly slaved within the bubble structure at the peak damage region. Compared with the irradiated Fe42 EHEA, the bubble distribution of Fe47 EHEA behaves quite differently. Firstly, the He bubbles are mostly distributed in a narrower range of 550–800 nm. Extra He bubbles can also be observed in the B2 phase deeper than 800 nm from the surface. Meanwhile, its average He bubble size is much smaller. The tiny He bubble in the B2 phase is hardly to be detected at the low magnification TEM image. The bubble population is also sparse. Overall, the BCC+B2 constituted Fe47 EHEA displayed a superior radiation tolerance to that of FCC + B2 constituted Fe42 EHEA, in terms of bubble formation.

To further study the irradiation responses of the different phases in the Fe42 and Fe47 EHEAs, the He bubble formation from surface to 900 nm in depth in the FCC, BCC, and B2 phases of Fe42 and Fe47 EHEAs were characterized in detail in the TEM images of Fig. 6. Generally, the He bubble size and number density depth-dependent and vary significantly with the phase structures in Fe42 and Fe47 EHEAs. The He bubble first emerged at a depth of ~270 nm for the B2 phase and 70 nm for the FCC structure in the Fe42 EHEA, and the He bubble size in the B2 phase is smaller than that of FCC phase. Compared with Fe42 EHEA, the B2 and BCC phases of Fe47 EHEA behaved different irradiation behaviors. Firstly, the He bubble first presented in the B2 phase and the BCC phase of the Fe47 EHEA at the depths of 420 nm, and 260 nm, respectively, which are deeper than that of Fe42 EHEA. Meanwhile, the He bubble in B2 phase of Fe47 EHEA shows the smallest size and number density among the phases in the Fe42 and Fe47 EHEAs.

To quantify the He bubbles distribution in the different phase structures of Fe42 and Fe47 EHEAs, the He bubble size and number

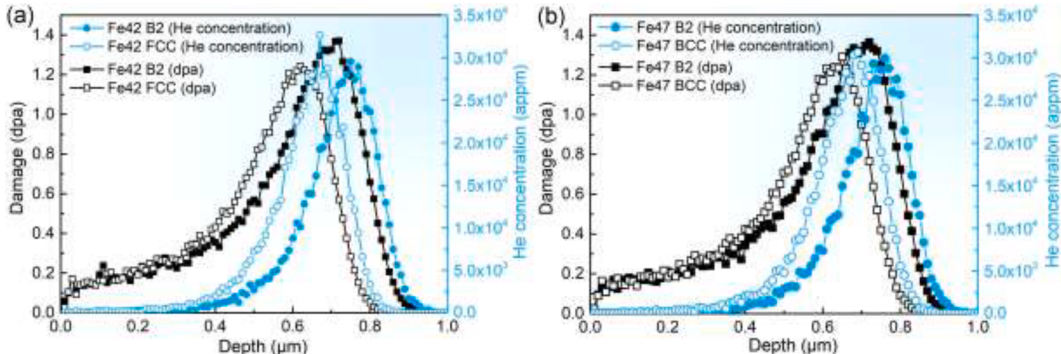


Fig. 1. The irradiation damage (dpa) and He concentration profiles of the FCC and B2 phases in Fe42 EHEA (a), and BCC, and B2 phases in Fe47 EHEA(b) calculated using SRIM.

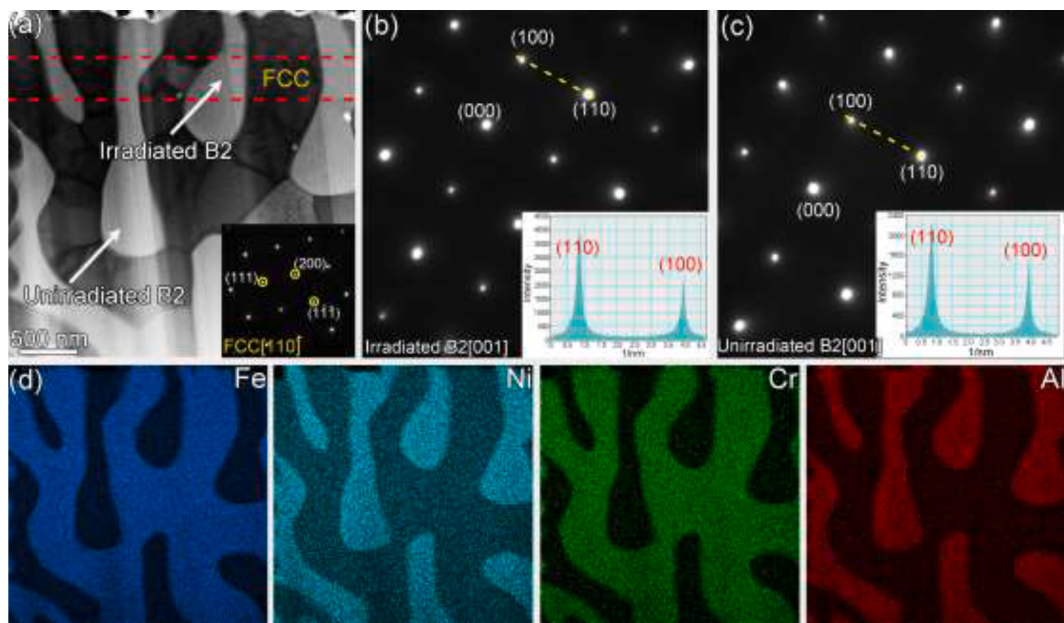


Fig. 2. Microstructural features and chemical compositions of the Fe42 EHEA after irradiation at 1073 K: (a) STEM-BF image showing the typical eutectic microstructure, the inset showing the SAED of the dark area confirming a FCC phase structure, (b) and (c) SAED patterns taken from the irradiation peak position and unirradiated area in Fig. 2(a), respectively, the insets in Fig. 2(b) and (c) showing the intensity profiles taken from the (100) superlattice spot and (110) diffraction spot outlined by the yellow dash line, (d) EDS maps showing the elements distribution of the disordered FCC phase and ordered B2 phase.

Table 1

Chemical compositions of the disordered FCC, BCC phases and ordered B2 phase in Fe42 and Fe47 EHEAs (at.%).

EHEA	Phase	Element			
		Fe	Ni	Cr	Al
Fe42	FCC	58.6	19.2	16.0	6.2
	B2	17.9	45.7	2.0	34.3
Fe47	BCC	62.3	14.7	15.3	7.7
	B2	19.4	38.9	2.3	39.4

density along the implantation depth were statistically analyzed, and the results were summarized in Fig. 7. In general, both the He bubble size and number density in Fe42 EHEA are larger than that of Fe47 EHEA in the depth range of 300–800 nm. For Fe42 EHEA, the maximum bubble sizes in FCC and B2 phases are 10.80 nm and 6.38 nm, respectively. While the maximum number densities of He bubbles in FCC and B2 phases are $3.33 \times 10^{22} / \text{m}^3$ and $3.90 \times 10^{22} / \text{m}^3$. The maximum bubble sizes in B2 and BCC phases of Fe47 EHEA are 2.74 nm and 5.10 nm, respectively. The number density of He bubbles in BCC phase of Fe47 EHEA shows a peak value of $2.94 \times 10^{22} / \text{m}^3$, which is smaller than that of Fe42 EHEA. Meanwhile, the volume swellings of He bubbles in different phases were calculated based on the following equation (Eq. (1)) [34].

$$\frac{\Delta V}{V} = \frac{4}{3} \pi (\bar{r})^3 \times \rho_n \quad (1)$$

where \bar{r} and ρ_n are the average radius and number density of the He bubble, respectively. Based on the experimental results, the overall volume swellings of FCC and B2 phases in Fe42 EHEA, BCC and B2 phases in Fe47 EHEA are 0.63%, 0.22%, 0.018%, 0.0075%, respectively. The smaller He bubble size, number density and volume swelling in Fe47 EHEA indicate that Fe47 EHEA has better anti-irradiation bubble nucleation and growth under 1073 K irradiation.

4. Discussion

The experimental results indicate that the Fe47 EHEA possesses a superior radiation tolerance than the Fe42 EHEA. In particular, the He bubbles in the B2 phase of Fe47 EHEA show smaller bubble sizes and fewer populations. The varied irradiation behaviors of the Fe42 and Fe47 EHEAs are believed to be controlled by their chemical compositions and microstructural features. It has been known that the He bubble nucleation and growth basically require He diffusion, which is the result of random jumps of He atoms from one lattice site to another [35]. The interstitial and substitutional sites (He atoms in vacancies) are the most important positions for He atoms in the crystal lattice. Thus, the migration modes of He atoms depend on temperature and the intrinsic or irradiation-induced defects, which can act as He atom traps [36]. Due to the rather low activation energy for interstitial diffusion, He atoms mainly diffuse through an interstitial mechanism at low temperatures ($T < 0.5 T_m$, where T_m is the melting point of the material), until they are trapped by another defect. Thus, the interstitial-type diffusion is only effective when the concentration of defects trapping He is negligibly small. Under the radiation at high temperatures ($T > 0.5 T_m$), the thermal vacancy concentration is significant, leading to the preferential substitutional sites for He atoms, due to the strong binding of He atoms to vacancies. Meanwhile, to reduce the strain energy in the lattice, vacancies tend to diffuse by preferentially exchanging with oversized atoms. Thus, the diffusion of He atoms at high temperatures ($T > 0.5 T_m$) can be achieved by exchanging positions between the large sized atoms and vacancies coupled with He atoms.

In this work, the Fe42 and Fe47 EHEAs were irradiated at 1073 K. The equilibrium concentration of interstitials is negligible at this temperature, while this is not the case for the vacancies. Significant vacancy concentration can be generated due to the coupled effects of thermal and irradiation. Thus, vacancy-dominated diffusion should be the main mechanism for helium bubble formation. Due to the limited solubility of He in alloys, the diffusion of He mainly coupled with vacancies to form bubbles. Thus, the vacancy behaviors, especially for the concentration and mobility, will have significant effects on the He behavior and bubble formation. the effective diffusivity of He atoms is expressed as follows [37]:

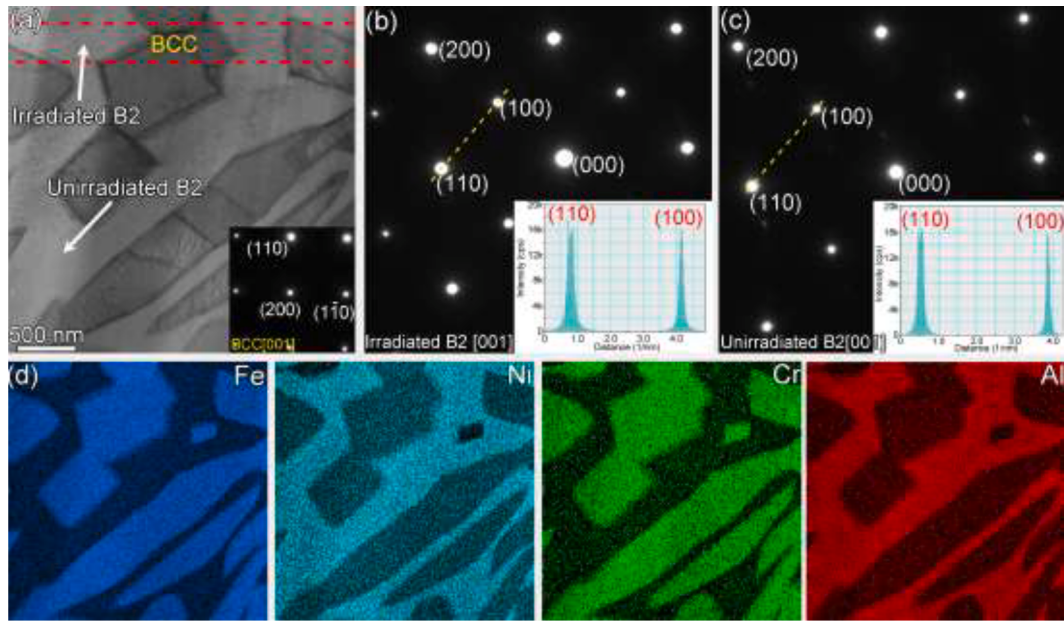


Fig. 3. Microstructural features and chemical compositions of the Fe47 EHEA after irradiation at 1073 K: (a) STEM-BF image showing the microstructure of Fe47 EHEA, the inset of the SAED pattern confirming a BCC phase structure of the gray area, (b) and (c) SAED patterns taken from irradiated and unirradiated B2 phases in Fig. 3(a), respectively, the insets in Fig. 3(b) and (c) showing the intensity profiles taken from the (110) diffraction spot and (100) superlattice spot outlined by the yellow dash line, (d) EDS maps showing the elements distribution of the disordered BCC and ordered B2 phases.

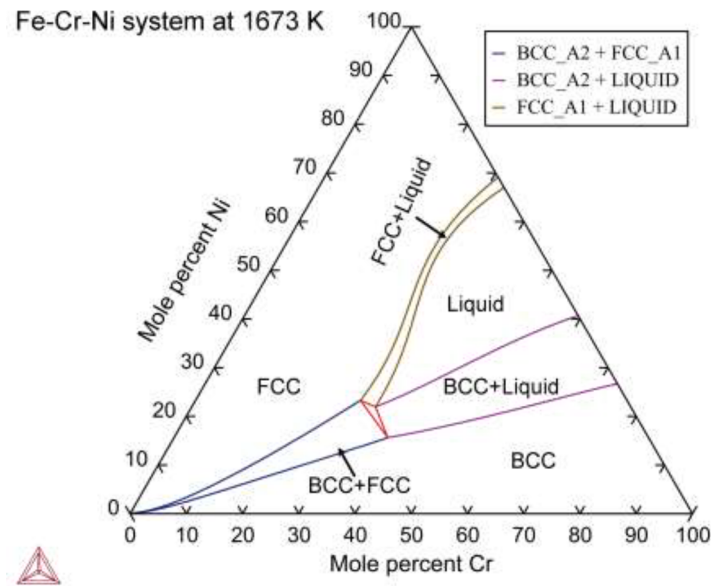


Fig. 4. Isothermal cross-sectional phase diagram of Fe-Cr-Ni system at 1673 K.

$$D_{He}^{eff} = C_V \times D_V \quad (2)$$

where C_V is the vacancy concentration, D_V is the vacancy diffusivity.

The vacancy concentration is mainly affected by the phase structure and phase composition of the EHEAs. Korhonen et al. compared the vacancy-formation energies between the FCC and BCC metals [38]. Generally, the materials with BCC crystal structure possess higher vacancy-formation energy than that of FCC-type materials, leading to a higher vacancy concentration in FCC phase [38]. More importantly, the chemical compositions also have significant effects on vacancy behavior. As mentioned above, the He diffusion mainly diffuses by combination with vacancies due to its low solubility in alloys. Meanwhile, to reduce the strain energy in the lattice, vacancies tend to diffuse

by preferentially exchanging with oversized atoms. Thus, the larger Fe and Cr atoms enriched in FCC phase can promote the diffusion of vacancies coupled with He, leading to easier growth of He bubbles. Although BCC phase is also rich in elements Fe and Cr, the BCC phase exhibits higher bubble swelling resistance than the FCC phase, which may be caused by the higher vacancy formation energy, reduced relaxation volume of BCC structure [39], and differences in solute trapping [40–42].

The responses of ordered B2 phase to irradiation are different with the disordered FCC or BCC phases. From the crystal structure point of view, the ordered B2 crystal structure possesses repulsive divacancy binding energy, leading to a reduction in the concentration of divacancies [43]. From the chemical composition point of view, the B2 phase

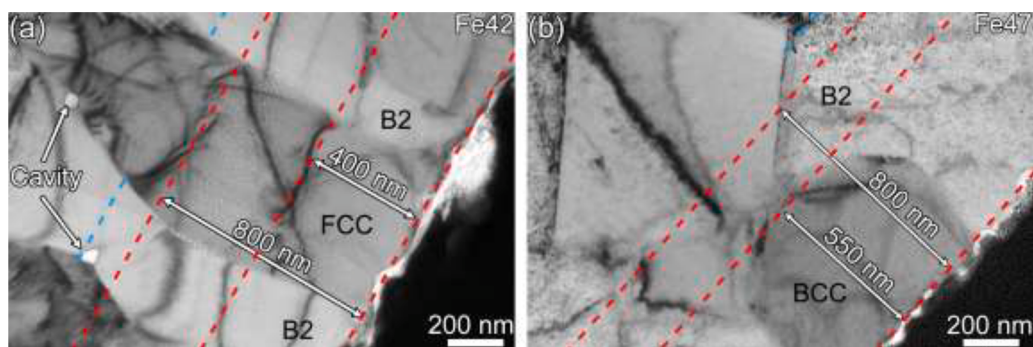


Fig. 5. (a) and (b) Low-magnification image showing the overall He bubble distribution in depth of Fe42 and Fe47 EHEA, respectively.

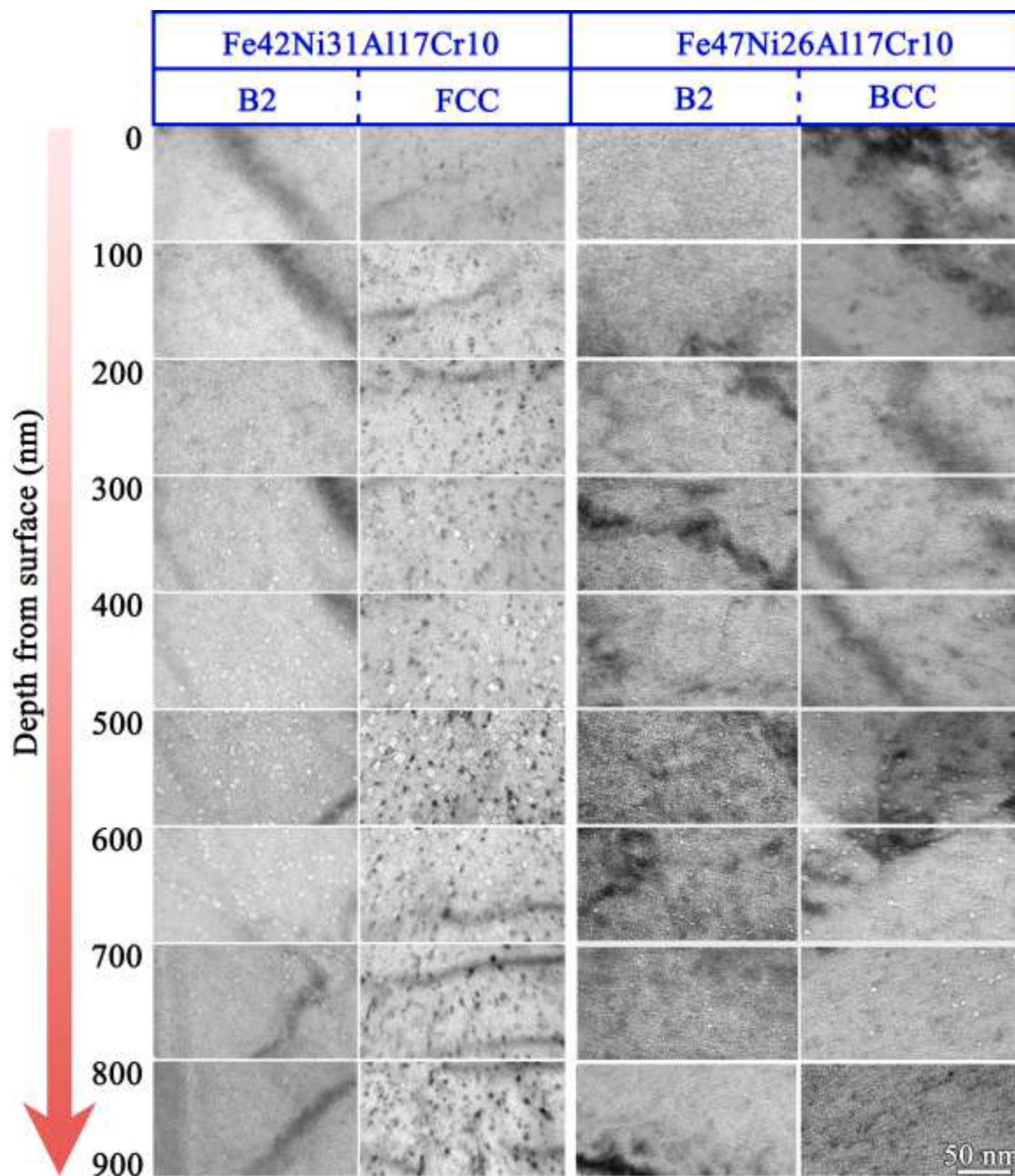


Fig. 6. TEM images showing the He bubble distributions from surface to 900 nm in depth in the FCC, BCC, and B2 phases of Fe42 and Fe47 EHEAs, which were irradiated by 275 keV He^+ at 1073 K.

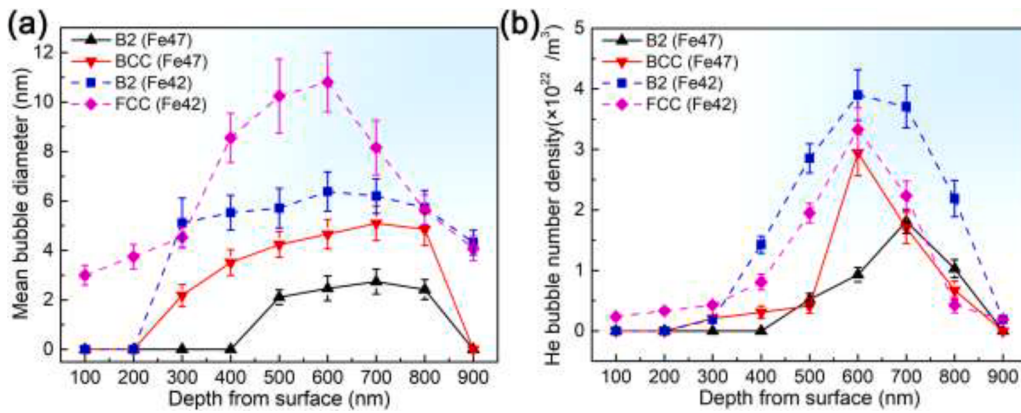


Fig. 7. Distribution of He bubble size and number density along with implantation depth of Fe42 and Fe47 EHEAs after irradiated at 1073 K: (a) He bubble size, (b) He bubble number density.

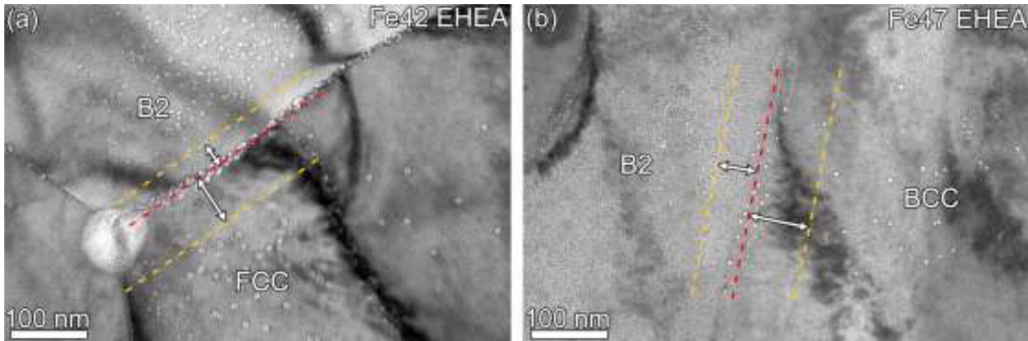


Fig. 8. Comparison of He bubbles in the phase boundary of peak region in Fe42 EHEA (a) and Fe47 EHEA (b).

is rich in elements Ni and Al, and depleted in elements Fe and Cr. Although Al possesses the largest metallic radius among the Fe, Cr, Ni Al atoms, it may be not easy for vacancies to exchange positions with Al atoms due to the strong chemical bonding between atoms in ordered B2 phase. Thus, the diffusion of He atoms bounded with vacancies was restrained. The slight decrease of ordering degree of B2 phase in Fe47 EHEA after irradiation demonstrated the strong chemical bonding between atoms and the resultant superior irradiation resistance.

To further illustrate the differences of vacancy diffusion in these phases, the bubble-denuded zone near the phase boundary was characterized. Because of the strong sink strength of boundary structure, the preference of vacancy migration towards the phase boundary shall leave a denuded zone for the radiation defect formation. It has been figured out that the width of the denuded zone is proportional to $\exp(-E_m/4kT)$, where E_m is the vacancy migration energy, k is a constant, T is the irradiation temperature. Therefore, in this work, a broader bubble-denuded zone means a lower vacancy migration energy of a specific phase. In Fig. 8, the bubble-denuded zones appeared near the phase boundaries in both Fe42 and Fe47 EHEAs. The denuded zone widths of B2 phases in Fe42 and Fe47 EHEAs are always smaller than those of FCC phase and BCC phase, respectively. More similar results can be observed in Fig. S.2. This indicated that B2 phase possesses higher vacancy migration energy, leading to a slower vacancy diffusion rate. Thus, the growth of He bubble can be suppressed in the ordered B2 phase. These results further supported the aforementioned inference on the He bubble formation resistance of the ordered B2 phase in the Fe47 EHEA.

5. Conclusions

In summary, two kinds of EHEAs were designed to study their responses to the He irradiation at 1073 K, i.e., $\text{Fe}_{42}\text{Ni}_{31}\text{Al}_{17}\text{Cr}_{10}$ and $\text{Fe}_{47}\text{Ni}_{26}\text{Al}_{17}\text{Cr}_{10}$. The phase composition and structure can be

controlled by adjusting the relative contents between Fe and Ni, which leads to different irradiation behaviors. In general, Fe47 EHEA containing B2 and BCC phases shows superior irradiation resistance to the Fe42 EHEAs containing B2 and FCC phases. The different responses to the irradiation are highly related to the vacancy dominated He diffusion behaviors, which are greatly affected by the phase compositions and structures. Oversized solute atoms tend to exchange with vacancies to promote the He diffusion, leading to a low irradiation resistance of FCC and BCC phases, which are rich in large-sized Fe and Cr. The slight decrease of ordering degree of B2 phase in irradiated Fe47 EHEA indicates a strong chemical bonding between Ni and Al atoms, which also contributes to a lower vacancy dominated He diffusion. The analysis on the width of bubble denuded zone along the phase boundary further suggested a higher energy barrier for the vacancy migration in the B2 phase. The findings of this work will provide guidance for the design of a new generation of radiation-resistant materials.

CRediT authorship contribution statement

Y.H. Zhou: Conceptualization, Investigation, Writing – original draft, Writing – review & editing. **S.F. Liu:** Conceptualization, Data curation. **D. Chen:** Funding acquisition. **Q.F. Wu:** Investigation. **B. Xiao:** Methodology. **F. He:** Writing – review & editing, Conceptualization. **Z.J. Wang:** Writing – review & editing, Conceptualization. **T. Yang:** Writing – review & editing. **J.J. Kai:** Project administration, Supervision.

Declaration of Competing Interest

The authors declare that they have no known competing financial interests or personal relationships that could have appeared to influence the work reported in this paper.

Data availability

Data will be made available on request.

Acknowledgment

This work was financially supported by Hong Kong Research Grant Council (RGC) [Grant Nos. CityU 11209021, 11214820 and C1017-21G], and China Fundamental Research Funds for the Central Universities with the project No. 3203002204A1 (Southeast University).

Supplementary materials

Supplementary material associated with this article can be found, in the online version, at [doi:10.1016/j.jnucmat.2023.154561](https://doi.org/10.1016/j.jnucmat.2023.154561).

References

- [1] M. Moschetti, P.A. Burr, E. Obbard, J.J. Kruzic, P. Hosemann, B. Gludovatz, Design considerations for high entropy alloys in advanced nuclear applications, *J. Nucl. Mater.* 567 (2022), 153814.
- [2] G. Was, D. Petti, S. Ukai, S. Zinkle, Materials for future nuclear energy systems, *J. Nucl. Mater.* 527 (2019), 151837.
- [3] B. Raj, M. Vijayalakshmi, P.V. Rao, K. Rao, Challenges in materials research for sustainable nuclear energy, *MRS Bull.* 33 (4) (2008) 327–337.
- [4] S.J. Zinkle, G. Was, Materials challenges in nuclear energy, *Acta Mater.* 61 (3) (2013) 735–758.
- [5] J. Koutský, J. Kocík, Radiation damage, J. Koutský, J. Kocík (Eds.), *Radiation Damage of Structural Materials*, Elsevier, 2013, pp. 22–63.
- [6] J. Hure, A. Courcelle, I. Turque, A micromechanical analysis of swelling-induced embrittlement in neutron-irradiated austenitic stainless steels, *J. Nucl. Mater.* 565 (2022), 153732.
- [7] L. Liu, X. Liu, Q. Du, H. Wang, Y. Wu, S. Jiang, Z. Lu, Local chemical ordering and its impact on radiation damage behavior of multi-principal element alloys, *J. Mater. Sci. Technol.* 135 (2023) 13–25.
- [8] S. Liu, G. Yeli, D. Chen, W. Lin, Y. Zhao, J. Luan, S. Zhao, T. Yang, J.J. Kai, NiCoCr-based medium-entropy alloys with superior resistance to radiation hardening and helium cavity growth, *J. Nucl. Mater.* 574 (2023), 154196.
- [9] M. Griffiths, Effect of neutron irradiation on the mechanical properties, swelling and creep of austenitic stainless steels, *Materials* 14 (10) (2021) 2622.
- [10] W. Lin, G. Yeli, G. Wang, J. Lin, S. Zhao, D. Chen, S. Liu, F. Meng, Y. Li, F. He, He-enhanced heterogeneity of radiation-induced segregation in FeNiCoCr high-entropy alloy, *J. Mater. Sci. Technol.* 101 (2022) 226–233.
- [11] T. Yang, Y. Zhao, Y. Tong, Z. Jiao, J. Wei, J. Cai, X. Han, D. Chen, A. Hu, J. Kai, Multicomponent intermetallic nanoparticle and superb mechanical behaviors of complex alloys, *Science* 362 (6417) (2018) 933–937.
- [12] Y. Zhou, Z. Zhang, D. Wang, W. Xiao, J. Ju, S. Liu, B. Xiao, M. Yan, T. Yang, New trends in additive manufacturing of high-entropy alloys and alloy design by machine learning: from single-phase to multiphase systems, *J. Mater. Inform.* 2 (4) (2022) 18.
- [13] Y. Zhao, F. Meng, T. Yang, J. Luan, S. Liu, G. Yeli, W. Lin, W. Liu, X. Liu, C. Liu, Enhanced helium ion irradiation tolerance in a Fe-Co-Ni-Cr-Al-Ti high-entropy alloy with L1₂ nanoparticles, *J. Mater. Sci. Technol.* 143 (2023) 169–177.
- [14] H. Zhang, C. Li, Z. Zhu, H. Huang, Y. Liu, T. Wang, T. Li, Effects of He-ion irradiation on the microstructures and mechanical properties of the novel Co-free V_xCrFeMnNi high-entropy alloys, *J. Nucl. Mater.* 572 (2022), 154074.
- [15] B. Cantor, I. Chang, P. Knight, A. Vincent, Microstructural development in equiatomic multicomponent alloys, *Mater. Sci. Eng. A* 375 (2004) 213–218.
- [16] F. Liu, P.K. Liaw, Y. Zhang, Recent progress with BCC-structured high-entropy alloys, *Metals* 12 (3) (2022) 501.
- [17] Y. Lu, Y. Dong, S. Guo, L. Jiang, H. Kang, T. Wang, B. Wen, Z. Wang, J. Jie, Z. Cao, A promising new class of high-temperature alloys: eutectic high-entropy alloys, *Sci. Rep.* 4 (1) (2014) 1–5.
- [18] Y. Tong, D. Chen, B. Han, J. Wang, R. Feng, T. Yang, C. Zhao, Y. Zhao, W. Guo, Y. Shimizu, Outstanding tensile properties of a precipitation-strengthened FeCoNiCrTi_{0.2} high-entropy alloy at room and cryogenic temperatures, *Acta Mater.* 165 (2019) 228–240.
- [19] Y. Zhang, G.M. Stocks, K. Jin, C. Lu, H. Bei, B.C. Sales, L. Wang, L.K. Béland, R. E. Stoller, G.D. Samolyuk, M. Caro, A. Caro, W.J. Weber, Influence of chemical disorder on energy dissipation and defect evolution in concentrated solid solution alloys, *Nat. Commun.* 6 (2015) 8736.
- [20] K. Jin, C. Lu, L. Wang, J. Qu, W. Weber, Y. Zhang, H. Bei, Effects of compositional complexity on the ion-irradiation induced swelling and hardening in Ni-containing equiatomic alloys, *Scr. Mater.* 119 (2016) 65–70.
- [21] C. Lu, L. Niu, N. Chen, K. Jin, T. Yang, P. Xiu, Y. Zhang, F. Gao, H. Bei, S. Shi, M. R. He, I.M. Robertson, W.J. Weber, L. Wang, Enhancing radiation tolerance by controlling defect mobility and migration pathways in multicomponent single-phase alloys, *Nat. Commun.* 7 (2016) 13564.
- [22] D. Chen, S. Zhao, J. Sun, P. Tai, Y. Sheng, Y. Zhao, G. Yeli, W. Lin, S. Liu, W. Kai, Diffusion controlled helium bubble formation resistance of FeCoNiCr high-entropy alloy in the half-melting temperature regime, *J. Nucl. Mater.* 526 (2019), 151747.
- [23] S. Zhao, D. Chen, J.J. Kai, First-principles study of He behavior in a NiCoFeCr concentrated solid-solution alloy, *Mater. Res. Lett.* 7 (5) (2019) 188–193.
- [24] Y. Lu, H. Huang, X. Gao, C. Ren, J. Gao, H. Zhang, S. Zheng, Q. Jin, Y. Zhao, C. Lu, A promising new class of irradiation tolerant materials: Ti₂ZrHfV_{0.5}Mn_{0.2} high-entropy alloy, *J. Mater. Sci. Technol.* 35 (3) (2019) 369–373.
- [25] S.J. Zinkle, L.L. Snead, Designing radiation resistance in materials for fusion energy, *Annu. Rev. Mater. Res.* 44 (2014) 241–267.
- [26] T. Lechtenberg, Irradiation effects in ferritic steels, *J. Nucl. Mater.* 133 (1985) 149–155.
- [27] S. Xia, X. Yang, T. Yang, S. Liu, Y. Zhang, Irradiation resistance in Al_xCoCrFeNi high entropy alloys, *JOM* 67 (10) (2015) 2340–2344.
- [28] J. Pang, T. Xiong, W. Yang, H. Ge, X. Zheng, M. Song, H. Zhang, S. Zheng, Atomic scale structure dominated FCC and B2 responses to He ion irradiation in eutectic high-entropy alloy AlCoCrFeNi_{2.1}, *J. Mater. Sci. Technol.* 129 (2022) 87–95.
- [29] G.S. Was, *The displacement of atoms. Fundamentals of Radiation Materials Science: Metals and Alloys*, Springer Berlin Heidelberg, Berlin, Heidelberg, 2007, pp. 73–124.
- [30] S.M. Allen, Foil thickness measurements from convergent-beam diffraction patterns, *Philos. Mag. A* 43 (2) (1981) 325–335.
- [31] M. Klinger, More features, more tools, more CrysTBox, *J. Appl. Crystallogr.* 50 (4) (2017) 1226–1234.
- [32] H. Zhang, C. Zhang, Q. Wang, C. Wu, S. Zhang, J. Chen, A.O. Abdullah, Effect of Ni content on stainless steel fabricated by laser melting deposition, *Opt. Laser Technol.* 101 (2018) 363–371.
- [33] I. Hemmati, V. Ocelík, J.T.M. De Hosson, Microstructural characterization of AISI 431 martensitic stainless steel laser-deposited coatings, *J. Mater. Sci.* 46 (2011) 3405–3414.
- [34] G.S. Was, Irradiation-induced voids and bubbles, *Fundamentals of Radiation Materials Science: Metals and Alloys*, Springer Berlin Heidelberg, Berlin, Heidelberg, 2007, pp. 379–484.
- [35] H. Trinkaus, B. Singh, Helium accumulation in metals during irradiation—where do we stand? *J. Nucl. Mater.* 323 (2–3) (2003) 229–242.
- [36] G.S. Was, Point defect formation and diffusion, *Fundamentals of Radiation Materials Science: Metals and Alloys*, Springer Berlin Heidelberg, Berlin, Heidelberg, 2007, pp. 167–205.
- [37] G.S. Was, Radiation-enhanced diffusion and defect reaction rate theory, *Fundamentals of Radiation Materials Science: Metals and Alloys*, Springer Berlin Heidelberg, Berlin, Heidelberg, 2007, pp. 207–252.
- [38] T. Korhonen, M.J. Puska, R.M. Nieminen, Vacancy-formation energies for fcc and bcc transition metals, *Phys. Rev. B* 51 (15) (1995) 9526.
- [39] J. Sniegowski, W. Wolfer, On the physical basis for the swelling resistance of ferritic steels, in: *Proceedings of the Topical Conference on Ferritic Alloys for Use in Nuclear Energy Technologies 17*, 1984, 17086893.
- [40] E. Little, D. Stow, Void-swelling in irons and ferritic steels: II. An experimental survey of materials irradiated in a fast reactor, *J. Nucl. Mater.* 87 (1) (1979) 25–39.
- [41] F. Garner, M. Toloczko, B. Sencer, Comparison of swelling and irradiation creep behavior of fcc-austenitic and bcc-ferritic/martensitic alloys at high neutron exposure, *J. Nucl. Mater.* 276 (1–3) (2000) 123–142.
- [42] E. Little, R. Bullough, M. Wood, On the swelling resistance of ferritic steel, *Proc. R. Soc. Lond. Ser. A Math. Phys. Sci.* 372 (1751) (1980) 565–579.
- [43] P. Munroe, The effect of nickel on vacancy hardening in iron-rich FeAl, *Intermetallics* 4 (1) (1996) 5–11.